

Crystallization of an exciton superfluid

J. Böning, A. Filinov,^{*} and M. Bonitz[†]

Institut für Theoretische Physik und Astrophysik, Christian-Albrechts-Universität, Leibnizstrasse 15, D-24098 Kiel, Germany

(Received 15 April 2011; revised manuscript received 20 July 2011; published 9 August 2011)

Indirect excitons—pairs of electrons and holes spatially separated in semiconductor bilayers or quantum wells—are known to undergo Bose-Einstein condensation and to form a quantum fluid. Here we show that this superfluid may crystallize upon compression. However, further compression results in quantum melting back to a superfluid. This unusual behavior is explained by the effective interaction potential between indirect excitons, which strongly deviates from a dipole potential at small distances due to many-particle and quantum effects. Based on first-principles path-integral Monte Carlo simulations, we compute the complete phase diagram of this system and predict the relevant parameters necessary to experimentally observe exciton crystallization in semiconductor quantum wells.

DOI: [10.1103/PhysRevB.84.075130](https://doi.org/10.1103/PhysRevB.84.075130)

PACS number(s): 71.35.Lk, 03.75.Hh, 05.30.Jp

I. INTRODUCTION

Quantum coherence of bosonic particles is one of the most striking macroscopic manifestations of the laws of quantum mechanics governing the microworld. The discovery of Bose-Einstein condensation in atomic vapors¹ was followed by the observation of condensation of bosonic quasiparticles in condensed matter—excitons. Here we mention early claims (though highly controversial) for three-dimensional (3D) semiconductors,² electron bilayers in a quantizing magnetic field,^{3,4} exciton polaritons in microcavities,^{5,6} and so-called indirect excitons formed from spatially separated electrons and holes.^{7–11} Not only was the bosonic gas phase observed, but also the formation of a quantum Bose liquid—an exciton superfluid with its peculiar loss of friction—could recently be verified.^{4,6} Thus it is tempting to ask whether there exists also a solid phase of bosons.

The key properties of a crystal are particle localization and long-range spatial ordering. To achieve spontaneous crystallization requires finding a Bose system with sufficiently strong and long-range pair interaction (here we do not consider particle localization induced by an external field in an optical lattice or cavity^{12,13}). However, the vast majority of previous experimental investigations have been performed in the regime of weak nonideality, where the interaction energy is small compared to the quantum kinetic energy. Therefore promising candidates for a bosonic solid are atoms or molecules with dipole interaction¹⁴ or excitons. Here, indirect excitons offer a number of attractive features: a strong dipole-type interaction, the suppression of biexciton or trion formation, the comparatively long radiative lifetime (on the order of microseconds), and the external controllability of the density and dipole moment via an electric field perpendicular to the quantum well plane.^{10,11,15}

In this paper we present clear evidence for the existence of a crystal of indirect excitons in semiconductor quantum wells. We compute its full phase diagram and reveal the parameters for its experimental verification. Our predictions are based on first-principles path-integral Monte Carlo (PIMC) simulations. But in contrast to previous quantum Monte Carlo studies, which predicted crystallization in model systems such as electron-hole bilayers,^{8,16} or two-dimensional dipole

systems,^{17,18} here we use realistic parameters typical for indirect excitons. In particular, we fully take into account the finite quantum well width, the composite character of the excitons, and the different masses of electrons and holes. This turns out to be of crucial importance for the exciton-exciton interaction, which strongly departs from a dipole potential at small distances. As a direct consequence we observe that the exciton crystal exists only in a finite density interval and undergoes quantum melting both at high and low density. Furthermore, when the exciton superfluid crystallizes to form a solid, quantum coherence is lost abruptly, i.e., there is no supersolid exciton phase.

This paper is organized as follows. In Sec. II we introduce the system of indirect excitons and present its reduced quasi-2D description. In Sec. III the effective exciton-exciton interaction potential is derived and its accuracy is verified. In Sec. IV we present our simulation results and the phase diagram of indirect excitons. Finally, we draw our conclusions in Sec. V.

II. MODEL

We consider a semiconductor quantum well (QW) of width L containing $N_e = N_h$ electrons and holes in the conduction and valence band, respectively, which are created by an optical pulse.¹⁹ Application of an electrostatic field of strength E perpendicular to the QW plane created, e.g., by a tip electrode allows us to spatially separate electrons and holes to different edges of the QW. By varying E this separation can be changed between 0 and L giving rise to a variable dipole moment d . At the same time, the field also provides lateral confinement and a variable particle density, via the quantum confined Stark effect, for details of the setup, see Sperlich *et al.*¹⁵ Finally, the system is kept in thermal equilibrium at a finite temperature T , which does not exceed a few percent of the binding energy of an electron-hole pair, thus all electrons and holes will be bound in $N = N_e$ indirect excitons.²⁰

The thermodynamic properties of this system are fully described by the density operator of N_e electrons and N_h holes, $\hat{\rho}_{N_e, N_h}^A = \mathcal{A}\{e^{-\beta\hat{H}}/Z\}$, where Z is the partition function, $\beta = 1/(k_B T)$, and \mathcal{A} denotes full antisymmetrization among all electronic and hole variables. The full Hamiltonian \hat{H}

contains kinetic energy, the interaction with the external electric field, and all Coulomb pair interactions between the $2N_e$ charged particles,

$$\hat{H} = \hat{H}_{\parallel} + \hat{H}_z + W, \quad (1)$$

with the single-particle contributions

$$\begin{aligned} \hat{H}_{\parallel} &= \sum_{i=1}^N \left[-\frac{\hbar^2 \nabla_{\mathbf{r}_i}^2}{2m_{e(h)}^{\parallel}} \right], \\ \hat{H}_z &= \sum_{i=1}^N \left[-\frac{\hbar^2 \nabla_{z_i}^2}{2m_{e(h)}^{\perp}} + V_{e(h)}^{QW}(z_i) + U_{e(h)}\{E_z\} \right], \end{aligned} \quad (2)$$

and the interaction part

$$\begin{aligned} W &= \sum_{i<j}^N V_{ij}^{\text{Coul}}, \\ V_{ij}^{\text{Coul}} &= \frac{e_i e_j}{\epsilon \sqrt{r_{ij}^2 + z_{ij}^2}}. \end{aligned} \quad (3)$$

Here r_{ij} denotes interparticle distances in the QW plane, V^{QW} is the QW confinement, U is the electrostatic potential energy due to the electric field and ϵ is the background dielectric constant, m^{\parallel} and m^{\perp} are the effective electron (hole) masses which take into account the anisotropy of the in-plane (out-of-plane) parabolic dispersions in the QW.

Under the present conditions of strongly bound indirect excitons with parallel dipole moments resulting in a strong exciton-exciton repulsion the very complicated evaluation of the density operator $\hat{\rho}_{N_e, N_h}^A$ can be substantially simplified. As was shown in Ref. 21 the system can be mapped onto N excitons, which can be treated as composite spin polarized bosons²² where deviations from the Bose statistics (arising from the original Fermi statistics of electrons and holes) have been found negligible.⁹ Thus the density operator is reduced to a fully symmetric one of N excitons, $\hat{\rho}_N^S$. Furthermore, all pair interactions can be properly averaged along the QW width giving rise to an effective (d -dependent) exciton-exciton interaction V_{XX} . As a result the system 2D Hamiltonian entering $\hat{\rho}_N^S$ becomes

$$\hat{H}^{\text{eff}} = \sum_{i=1}^N \left[-\frac{\hbar^2 \nabla_{\mathbf{r}_i}^2}{2m_X} \right] + \sum_{i<j} V_{XX}(r_{ij}; d), \quad (4)$$

where $m_X = m_e^{\parallel} + m_h^{\parallel}$ is the in-plane effective mass, \mathbf{r}_i is the in-plane center-of-mass (c.m.) coordinate of the i th exciton, and $r_{ij} = |\mathbf{r}_i - \mathbf{r}_j|$ denotes the c.m. distance between two excitons.

Below we use atomic units, i.e., lengths will be given in units of the electron Bohr radius, $a_B^* = \hbar^2 \epsilon / (e^2 m_e^{\parallel})$, and energies in units of the electron Hartree, $\text{Ha}^* = e^2 / (\epsilon a_B^*)$. In particular, for the indirect excitons in $\text{ZnS}_x\text{Se}_{1-x}/\text{ZnSe}$ QW with the doping factor $x = 0.3$, we use $m_e^{\parallel}/m_0 = 0.15$, $\epsilon = 8.7$, which results in $a_B^* = 3.07$ nm and the energy unit $\text{Ha}^* = 53.93$ meV.

III. EFFECTIVE INTEREXCITON INTERACTION

To verify the approximation (4) and the validity of the potential V_{XX} we consider the two-exciton (biexciton) problem. We define the exciton interaction energy as the energy difference of a biexciton and two single excitons, $E_{XX}(r_{hh}) = E_{2X}(r_{hh}) - 2E_X$, which depends parametrically on the distance between the holes in a biexciton problem, $r_{hh} = |\mathbf{R}_1 - \mathbf{R}_2|$. The distance r_{hh} remains a well defined quantity also at small interexciton separations, when a strong overlap of the exciton wave functions and particle exchange takes place. In this case the c.m. distance is not physical. The substitution of r_{ij} in Eq. (4) by r_{hh} can be justified as follows.

Similar to the hydrogen problem, the single exciton wave function can be factorized into the c.m. and the relative part,

$$\Psi(\mathbf{r}, \mathbf{R}) = \Psi_C(\mathbf{R}^0) \Psi_r(|\mathbf{r} - \mathbf{R}|), \quad (5)$$

with

$$\begin{aligned} \mathbf{R}^0 &= \frac{m_e}{m_X} \mathbf{r} + \frac{m_h}{m_X} \mathbf{R}, \\ m_X &= m_e + m_h, \end{aligned} \quad (6)$$

where the vectors \mathbf{r} , \mathbf{R} , and \mathbf{R}^0 denote the electron, hole, and c.m. coordinates, respectively.

The relative part Ψ_r can be found by solving a single-particle problem with the reduced mass $\mu = m_e m_h / (m_e + m_h)$ in the potential, $V_d = -e^2 / \sqrt{|\mathbf{r} - \mathbf{R}| + d^2}$, where the z direction is taken into account explicitly by the layer separation d , which is nothing but the exciton dipole moment (divided by the elementary charge $|e|$). Therefore we will use the notion dipole moment for d in the following. For the spatially indirect exciton we approximate

$$V_d|_{r<d} = -\frac{e^2}{\sqrt{r^2 + d^2}} \approx -\frac{e^2}{d} \left(1 - \frac{r^2}{2d^2} + \dots \right), \quad (7)$$

$$\Psi_r^H(\mathbf{r})|_{r<d} \propto e^{-r^2/2l^2}, \quad l^2 = \frac{\hbar}{\mu\omega}, \quad \omega^2 = \frac{e^2}{\mu d^3}, \quad (8)$$

i.e., the leading term of the expansion describes a harmonic oscillator and the relative part near the exciton origin decays as a Gaussian. Now, using the definition of \mathbf{R}^0 and the substitution, $(\mathbf{r} - \mathbf{R}) = \gamma_m(\mathbf{R}^0 - \mathbf{R})$ with $\gamma_m = m_X/m_e$, the relative part can be expressed solely in terms of the hole coordinate (keeping the c.m. coordinate \mathbf{R}^0 as a fixed parameter),

$$\Psi(\mathbf{r}, \mathbf{R}) = \Psi_C(\mathbf{r}, \mathbf{R}) \Psi_r(\mathbf{R}, \mathbf{R}^0), \quad (9)$$

where the relative part (8) contains a factor γ_m^2 in the exponent, $\Psi_r^H(\mathbf{r})|_{r=|\mathbf{R}^0-\mathbf{R}|} \propto e^{-\gamma_m^2 r^2/l^2}$. For a typical electron-hole mass ratio in semiconductors, $\gamma_m \sim 2 \dots 4$, we conclude that the hole is well localized around the c.m.. This allows us to make a second step.

We treat the excitons in the Born-Oppenheimer (BO) approximation and apply the adiabatic transformation for the spatial part of the full wave function. Spin degrees of freedom are omitted in the present analysis because they are of minor importance and their treatment would require substantially more elaborate simulations. In fact, our model for the exciton interaction potential has a significantly larger effect on the

results. Therefore in the derivation of the effective potential we start with the following two-exciton wave function (coordinate part):²³

$$\Psi_{XX} = \frac{1}{(2!)^2} \sum_{P_e, P_h} (\pm 1)^{\delta P_e + \delta P_h} \Psi_e(\hat{P}_e \mathbf{r}_1, \hat{P}_e \mathbf{r}_2, \mathbf{R}_1, \mathbf{R}_2) \times \Psi_h(\hat{P}_h \mathbf{R}_1, \hat{P}_h \mathbf{R}_2), \quad (10)$$

which can be symmetric or antisymmetric depending on the symmetry of the spin part. The action of the electron and hole permutation operators, $\hat{P}_{e(h)}$, explore all exchange possibilities (excluding the electron-hole exchange). Within this ansatz one can self-consistently solve the Schrödinger equations for the electrons,

$$\hat{H}_e \Psi_e^{(n)}(\mathbf{r}_1, \mathbf{r}_2, \mathbf{R}_1, \mathbf{R}_2) = E_e^{(n)}(\mathbf{R}_{12}) \Psi_e^{(n)}(\mathbf{r}_1, \mathbf{r}_2, \mathbf{R}_1, \mathbf{R}_2), \quad (11)$$

and holes

$$\begin{aligned} & [\hat{H}_h + E_e^{(n)}(\mathbf{R}_{12})] \Psi_h^{(m)}(\mathbf{R}_1, \mathbf{R}_2, \mathbf{R}_1^0, \mathbf{R}_2^0) \\ &= E_{2X}^{(m)} \Psi_h^{(m)}(\mathbf{R}_1, \mathbf{R}_2, \mathbf{R}_1^0, \mathbf{R}_2^0), \end{aligned} \quad (12)$$

where

$$\begin{aligned} \hat{H}_e &= \sum_{i=1,2} [\hat{T}_e^i + V_{eh}(\mathbf{r}_i - \mathbf{R}_1) + V_{eh}(\mathbf{r}_i - \mathbf{R}_2)] \\ &+ V_{ee}(\mathbf{r}_1 - \mathbf{r}_2), \end{aligned} \quad (13)$$

$$\hat{H}_h = \sum_{j=1,2} \hat{T}_h^j + V_{hh}(\mathbf{R}_{12}), \quad (14)$$

$$\hat{T}_{e(h)} = -\frac{\hbar^2 \nabla^2}{2m_{e(h)}}, \quad (15)$$

with $n, m \in \{A, S\}$ being defined by the symmetry of the electron (hole) wave function, and $E_e^{(n)}$ being an additional mean-field electron potential influenced by the holes in the biexciton.

If the holes are treated as infinitely heavy,²⁴ the numerical solution of Eq. (12) is not necessary and the biexciton energy can be decomposed, $E_{2X} = E_e^{(n)}(r_{hh}) + V_{hh}$, with $V_{hh} = e^2/|r_{hh}|$. The electron contribution $E_e^{(n)}$ is the solution for a singlet (triplet) state,

$$\begin{aligned} & \left[\sum_{i=1,2} \left(-\frac{\hbar^2 \nabla_{r_i}^2}{2m_e} + V_{eh}(\mathbf{r}_i) \right) + \frac{e^2}{|\mathbf{r}_1 - \mathbf{r}_2|} \right] \Psi_e^{S/A} \\ &= [E_e^{S/A} + 2E(X)] \Psi_e^{S/A}, \end{aligned} \quad (16)$$

where

$$V_{eh}(\mathbf{r}_i) = \sum_{j=1}^2 -\frac{e^2}{\sqrt{(\mathbf{r}_i + \mathbf{R}_j)^2 + d^2}}, \quad (17)$$

with the holes located at $\mathbf{R}_{1,2} = \pm \frac{1}{2} \mathbf{r}_{hh}$. This equation has been solved numerically for an experimentally feasible e-h separation $d = 13.3a_B^*$.²⁵ A first observation is that the energy $E_e(m_h \rightarrow \infty)$ is not sensitive to r_{hh} , once $r_{hh} \lesssim d$; see Fig. 1(a). This is understood from the behavior of the electron density [see Fig. 1(b)]: in all cases the electron cloud extends well beyond r_{hh} , which is a result of the shallow interaction

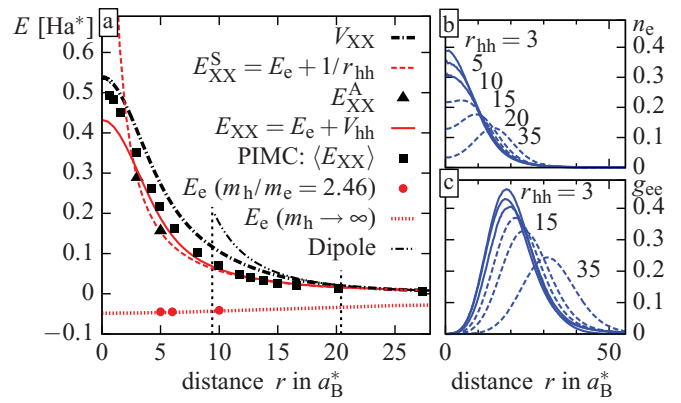


FIG. 1. (Color online) Exciton interaction potential V_{XX} for a dipole moment $d = 13.3a_B^*$. (a) The interaction potential V_{XX} (point-dashed line) is compared to the exciton interaction energy E_{XX} in several approximations: average interaction of two excitons ($\langle E_{XX} \rangle$) evaluated by PIMC simulations using the Hamiltonian, Eq. (4); the BO model with the infinite hole mass, symmetric (E_{XX}^S), and antisymmetric (E_{XX}^A) electronic states; the improved BO model, $E_{XX} = E_e + V_{hh}$, with a realistic mass ratio $m_h/m_e = 2.46$ (ZnSe-based QW). Also shown are the electronic contribution E_e and the dipole potential d^2/r^3 . Two vertical lines indicate the boundaries of the exciton crystal. (b) Radial electron density $n_e(r)$ for several hole separations r_{hh} , relative to the midpoint of two holes located at $\mathbf{R}_{1,2} = \pm \frac{1}{2} \mathbf{r}_{hh}$. (c) Electron pair distribution function $g_{ee}(r_{ee})$ for the values r_{hh} in (b).

potential, $V_{eh}(r)$, of an electron with the two holes for $r_{hh} < d$, and the strong e-e repulsion that keeps the electrons at an average distance $\tilde{r} \sim 20a_B^*$ apart, practically independent on the hole-hole separation. This behavior is evident from the pair distribution function $g(r_{ee})$; see Fig. 1(c). Consequently, for a large exciton dipole moment, we observe no noticeable difference in the energy of the symmetric and antisymmetric states, merging into a single curve $E_e(m_h \rightarrow \infty)$; see Fig. 1(a). With these results we can now analyze $E_{XX}(r_{hh})$, cf. red dashed line in Fig. 1(a). At large distances, $r \gtrsim d$, E_{XX} practically coincides with the classical dipole potential, $V_D = d^2/r^3$, so we expect the system to behave like 2D polarized dipoles, at low densities. At smaller distances, $r < d$, however, E_{XX} essentially follows a Coulomb potential which arises mainly from the hole-hole repulsion. Finally, for $r \ll d$, the interaction energy shows an unphysical Coulomb singularity originating from the assumption of an infinite hole mass. In real systems, E_{XX} is expected to be softer, approaching a finite value at zero distance, due to quantum diffraction and exchange effect, similar to the behavior of the Kelbg potential in 3D electron-ion plasmas.^{26–28} Therefore we proceed with the generalization of the model for a finite hole mass.

In the situation with a large dipole moment, as considered in Fig. 1(a), the interaction energy is positive at all distances and hence no bound states (biexcitons) are formed. This originates from the positive eigenvalues of the Schrödinger equation for the holes (12). Therefore evaluation of the interaction energy should not be limited only to the ground-state solution of Eq. (12), but should include contributions of all states,

including the continuum.²⁹ This can be done directly via the two-particle partition function Z_2 ,

$$Z_2(\beta, r_{\text{hh}}) = \int d\mathbf{R}_1 d\mathbf{R}_2 \rho(\mathbf{R}_1, \mathbf{R}_2; \mathbf{R}_1, \mathbf{R}_2; \beta) \times \delta(|\mathbf{R}_1 - \mathbf{R}_2| - r_{\text{hh}}), \quad (18)$$

the density matrix, and the thermodynamic energy estimator

$$E(r_{\text{hh}}) = -\frac{\partial}{\partial \beta} \ln Z_2(\beta, r_{\text{hh}}). \quad (19)$$

Here, Z_2 parametrically depends on the distance r_{hh} between the particles. Applied to the case of two holes in the biexciton ($E \equiv E_{2X}$), the density matrix is the solution of the two-body Bloch equation with the Hamiltonian, $\hat{H}_h + E_e^{(n)}(|\mathbf{R}_1 - \mathbf{R}_2|)$, see Eq. (12), which can be factorized into the c.m. free particle density matrix and the relative part,

$$\rho(\mathbf{R}_1, \mathbf{R}_2; \mathbf{R}'_1, \mathbf{R}'_2; \beta) = \rho_F(\mathbf{R}_c, \mathbf{R}'_c; \beta) \rho(r_{\text{hh}}, r'_{\text{hh}}; \beta), \quad (20)$$

where

$$\rho(r_{\text{hh}}, r'_{\text{hh}}; \beta) \equiv \rho_F(r_{\text{hh}}, r'_{\text{hh}}; \beta) e^{-U^{\text{eff}}(r_{\text{hh}}, r'_{\text{hh}}; \beta)}. \quad (21)$$

Here U^{eff} is the effective pair action,^{26,28} introduced in a way that at large distances and (or) high temperatures it reduces to $\beta[e^2/|r_{\text{hh}}| + E_e^{(n)}(r_{\text{hh}})]$. Substituted in Eqs. (18) and (19) we obtain

$$E_{2X}(r_{\text{hh}}; \beta) = k_B T + \left(k_B T + \frac{\partial}{\partial \beta} U^{\text{eff}}(r_{\text{hh}}, r_{\text{hh}}; \beta) \right), \quad (22)$$

where the first term accounts for the c.m. kinetic energy (in two dimensions). For spherically symmetric potentials the effective action and its temperature derivative can be evaluated with the matrix-squaring technique.^{30,31} The resulting interaction energy, $E_{XX}(r_{\text{hh}}; \beta) = E_{2X}(r_{\text{hh}}; \beta) - E_X(\beta)$, evaluated at the temperature $1/\beta = 10^{-3} \text{ Ha}^*$ is shown in Fig. 1(a) by the red solid line. Quantum effects arising from the finite hole mass (e.g., for the ZnSe-based QWs, $m_h/m_e \simeq 2.46$) strongly affect the interaction energy E_{XX} for $r < 3a_B^*$, which consequently approaches a finite value at zero distance.

For final comparison, we compute the exciton interaction energy by PIMC simulations using the Hamiltonian (4). We used two bosonic excitons of mass m_X in periodic boundary conditions. The result, $\langle E_{XX} \rangle$, as a function of the average interexciton distance, $\langle r \rangle = \int d\mathbf{r} r g(r) \cdot [\int d\mathbf{r} g(r)]^{-1}$, evaluated via the exciton pair distribution function $g(r)$, is shown in Fig. 1(a) by the solid squares. This quantity agrees well with the finite-mass BO solution, E_{XX} , for $r_{\text{hh}} > 5a_B^*$, and confirms applicability of both models in the density range where we predict formation of the excitonic crystal. The deviations being noticeable at smaller distances are outside the density range used in the present analysis.

IV. SIMULATION RESULTS

Using PIMC simulations with $\hat{\rho}_N^s$ and the Hamiltonian (4) the thermodynamic properties of the N strongly correlated excitons can be efficiently computed with full account of all interactions, quantum and spin effects, without further approximations. Of central importance for the crystallization is the coupling (nonideality) parameter, i.e., the ratio of interaction energy to kinetic energy. For a quantum system

with Coulomb (dipole) interaction it is given by the Brueckner parameter r_s (the dipole coupling parameter D),

$$r_s \equiv \frac{a}{a_B^*} \sim n^{-1/2}, \quad D \equiv \frac{M_X}{m_e^{\parallel}} \frac{1}{\sqrt{\pi} r_s} \frac{d^2}{a_B^{*2}} \sim n^{1/2}, \quad (23)$$

where a is the mean interparticle distance and n is the exciton density. Note the opposite scaling of r_s and D with density.

We perform 2D grand-canonical PIMC simulations³² with periodic boundary conditions and extract the results for the canonical ensemble with $N = 60-500$ excitons. To map out the phase diagram we scan a broad parameter range spanning three orders of magnitude of density and temperature. We first obtain the phase diagram for a fixed value of the dipole moment, corresponding to $d = 13.3a_B^*$, and after that we analyze in Sec. VB how the crystal phase boundary changes when d is varied.

A. Spatial ordering of excitons

To detect crystallization we compute the exciton pair distribution function (PDF), $g(\mathbf{r})$. This function is homogeneous in an ideal gas, whereas in the fluid and crystal phase it exhibits increasing modulations, which signal localization and spatial ordering. Typical examples of $g(\mathbf{r})$ are displayed in the top rows of Figs. 2 and 4 and show clear evidence of exciton localization. The existence of the translational long-range order (LRO) is detected from the asymptotic behavior of the angle-averaged function $g(r)$ for large $r = |\mathbf{r}|$. In two dimensions a possible freezing scenario is given by the Kosterlitz-Thouless-Nelson-Halperin-Young (KTNY) theory (see the overview³³), predicting an exponential (algebraic) decay of the peak heights of $g(r)$ above (below) the melting temperature.

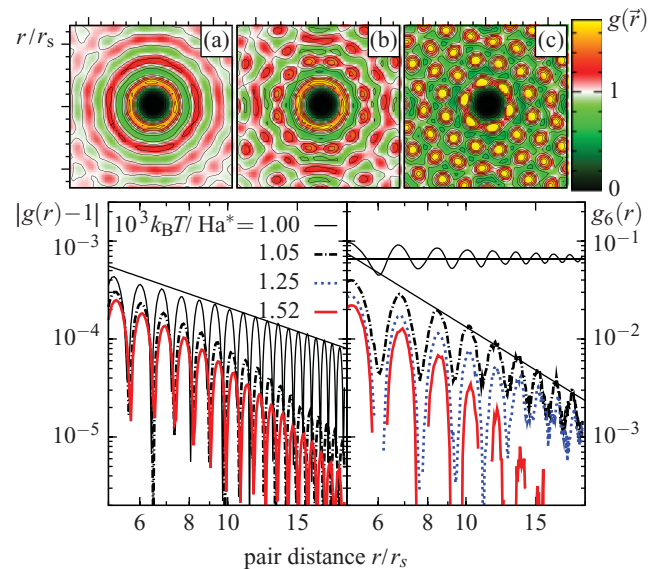


FIG. 2. (Color online) Constant density freezing. Top row: 2D PDF $g(r_{ij})$ (relative to a fixed particle in the center) for $na_B^{*2} = 0.0035$ and temperatures $k_B T/\text{Ha}^*$ of 1.74×10^{-3} (a), 1.38×10^{-3} (b) and 1.08×10^{-3} (c). Bottom: Radial distribution function $|g(r) - 1|$ (left) and bond angular order distribution function $g_6(r)$ (right) at $na_B^{*2} = 0.0022$ for $N = 500$. Lines are a guide to the eye to visualize an algebraic decay in this log-log plot.

Indeed, our simulations find some support for this scenario; see bottom left part of Fig. 2.

The existence of angular hexagonal LRO follows from the asymptotic behavior of the bond angular correlation function, $g_6(r) = \langle \psi_6^*(r) \psi_6(0) \rangle$, with $\psi_6(r_k) = n_l^{-1} \sum_{l=1}^{n_l} e^{i6\Theta_{kl}}$, where n_l is the number of nearest neighbors of a particle located at r_k , and Θ_{kl} is their angular distance. We observe a change from an exponential asymptotic of g_6 to a constant, which is the expected behavior for a liquid-solid transition; see the bottom-right part of Fig. 2. There are some indications for the existence of a hexatic phase—coexistence of angular quasi-LRO (algebraic decay) and missing translational LRO in a narrow temperature interval; see curves for $k_B T = 1.05 \times 10^{-3} \text{ Ha}^*$ and $k_B T = 1.25 \times 10^{-3} \text{ Ha}^*$.

In addition we performed a Voronoi analysis, which provides access to local distortions of the hexagonal symmetry of the lattice. The average fraction of particles (the probability) with a number of nearest neighbors deviating from 6 is referred to as the defect fraction, i.e., $(1 - P_6)$. The results of Fig. 3 explore the nature of the melting transition at constant density. We observe a sharp increase of the number of defects at the melting point, which is in disagreement with the KTNHY scenario. A possible alternative to the KTNHY is a first-order solid-liquid phase transition, with an exponential decay of $g_6(r)$. However, the latter was not observed in our simulations, possibly due to a limited system size ($N \sim 500$). The constructed Voronoi map for different particle configurations shows the accumulation of the defects at the boundaries between few crystallites. A similar picture, but for a significantly larger classical system ($N \sim 10^6$) has been recently reported and the transition was proved to be of first order.³⁴ If that system was equilibrated sufficiently long, the intermediate hexatic phase completely vanished. With our

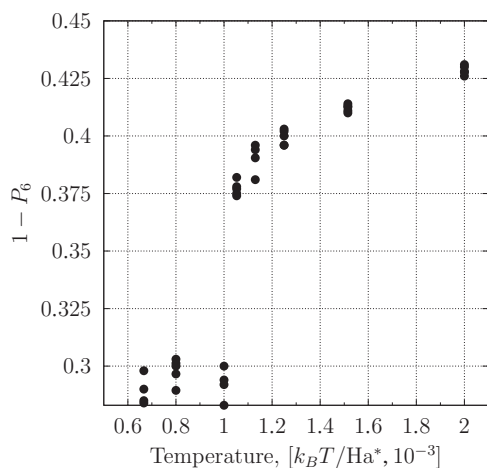


FIG. 3. Temperature dependence of the defect fraction at density $na_B^{*2} = 2.2 \times 10^{-3}$ and particle numbers $N = 501-505$ (vertically aligned dots) characterizing the ordered and disordered phases. The defect fraction $(1 - P_6)$ shows a sharp jump at $T \sim 10^{-3} \text{ Ha}^*$. This is in disagreement with the KTNHY theory, which predicts a continuous unbinding of dislocations in the hexatic phase indicated by a continuous variation of the critical exponent $\eta_6(T) \leq 1/4$ and the bond angular correlation function $g_6(r) \sim r^{-\eta_6(T)}$. In contrast, we observe an abrupt transition from the LR angular order ($T < T_c$) to a quasi-long-range angular order with $\eta_6(T) \sim 2$ ($T \geq T_c$); see Fig. 2.

data for the limited particle numbers we cannot give a confident answer whether we observe a discontinuous transition in the present system.

B. Exciton quantum coherence: Superfluidity

After analyzing emergence of *spatial ordering* let us turn to the *quantum coherence* properties of nonideal indirect excitons. In a 2D Bose system cooling leads to sudden emergence of coherence in the liquid phase—the normal fluid—superfluid transition. The phase boundary is governed by the Berezinskii-Kosterlitz-Thouless (BKT) scenario³⁵ and is given by the condition $\chi = 4/\gamma_s$ for the exciton quantum degeneracy parameter $\chi \equiv n\Lambda^2$,

$$k_B T_{\text{KT}}(n_s) = \frac{\pi}{2} n_s \frac{m_c^{\parallel}}{m_X} \text{Ha}^*, \quad (24)$$

where $n_s = \gamma_s n$ is the exciton superfluid density. Therefore a key quantity is the superfluid fraction γ_s , where $0 \leq \gamma_s \leq 1$. In PIMC simulations, it is directly computed from the statistics of the winding number W :³⁶

$$\gamma_s = \frac{m_X}{N\hbar^2\beta} \langle W^2 \rangle, \quad \mathbf{W} = \sum_{i=1}^N \int_0^\beta dt \frac{d\mathbf{r}_i(t)}{dt}. \quad (25)$$

Typical simulation results for γ_s are shown in the bottom part of Fig. 4.

Figure 5 illustrates the computation of the winding number versus temperature (left) and the finite-size scaling for the critical temperature T_{KT} of the BKT transition (right). One observes a systematic shift of $T_{\text{KT}}(N)$ to lower values with an increase of the system size N . The extrapolation to

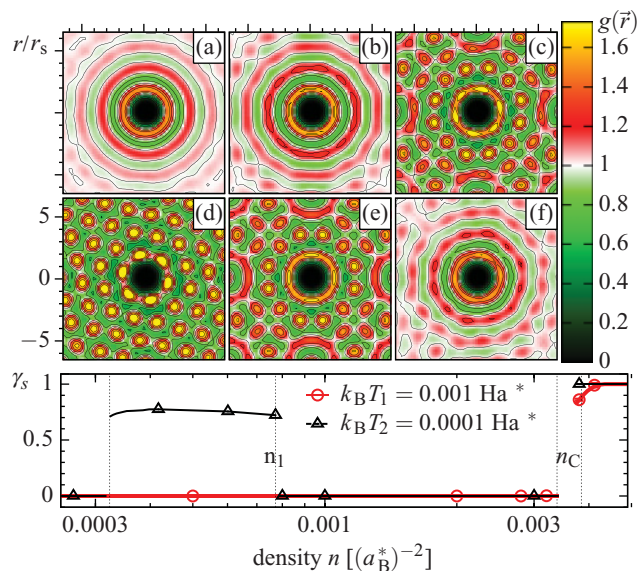


FIG. 4. (Color online) Isothermal freezing and melting of indirect excitons. (a)–(f) 2D PDF $g(r)$ for $k_B T_1 = 0.001 \text{ Ha}^*$ at densities na_B^{*2} of 0.84×10^{-3} (a), 1.3×10^{-3} (b), 1.7×10^{-3} (c), 3.2×10^{-3} (d), 3.6×10^{-3} (e), and 4.0×10^{-3} (f). Bottom panel: Superfluid fraction γ_s , Eq. (25), vs density for two temperatures. Symbols are PIMC results, lines are a guide to the eye. The increase of γ_s at high density extends over a small finite range of solid-liquid coexistence, which is due to the finite particle number in the simulations.

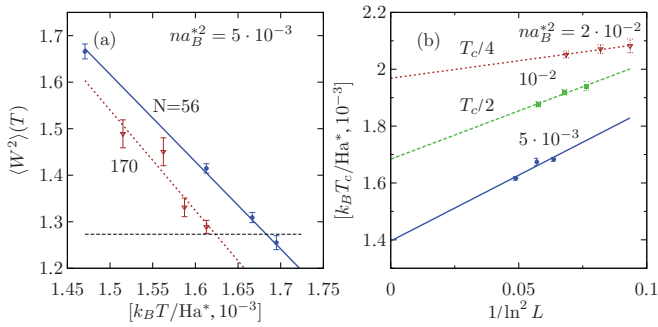


FIG. 5. (Color online) (a) Temperature dependence of the winding number $\langle W^2 \rangle(T)$ for the exciton numbers $N = 56$ and 170 . Density $na_B^{*2} = 5 \times 10^{-3}$. The Berezinskii-Kosterlitz-Thouless transition temperature $T_{KT}(N)$ is determined by the condition (Refs. 18 and 35) $\langle W^2 \rangle(T_{KT}) = 4/\pi$, shown by the horizontal dashed line. (b) System size dependence of $T_{KT}(L)$ for three densities: $na_B^{*2} = 5 \times 10^{-3}$, 10^{-2} , and 2×10^{-2} . Values of T_{KT} are rescaled to fit into a single plot.

the thermodynamic limit, $T_{KT}(L \rightarrow \infty)$, with $L = \sqrt{N/n}$, is obtained by fitting the simulation data by the equation $T_{KT}(L) = T_{KT}(\infty) + b/\ln^2(L)$. It is a direct consequence of the Kosterlitz-Thouless renormalization-group analysis,³⁵ which is considered to be exact in the asymptotic regime of large L . This scaling allows us to make predictions for the phase-transition line in a macroscopic system.

C. Phase diagram of indirect excitons

We now summarize our findings in the complete phase diagram of indirect excitons in the density-temperature plane, which is presented in Fig. 6. The degeneracy line $\chi = 1$ separates the regions of classical (above the line) and quantum

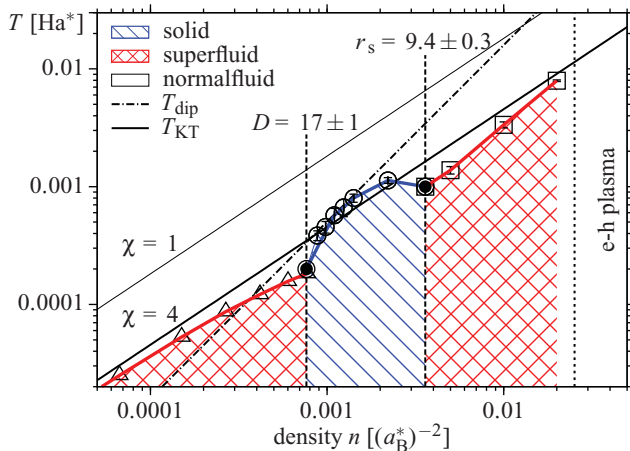


FIG. 6. (Color online) Phase diagram of 2D indirect excitons with $d = 13.3a_B^*$. Circles and squares mark our PIMC results, data for triangles are from Ref. 18. Vertical dashed lines ($D = 17 \pm 1$ and $r_s = 9.4 \pm 0.3$) indicate the two density induced quantum freezing (melting) transitions. Filled symbols mark the two triple points. The normal-fluid–superfluid phase boundary is marked by the full (red) line with triangles and squares, respectively, and is below the ideal estimate T_{KT} according to Eq. (24); cf. thick solid line labeled $\chi = 4$. The line T_{dip} marks the freezing transition of a classical 2D dipole system. The e-h plasma phase is beyond the present analysis.

behavior (below). While classical excitons exist only in a fluid (or gas) phase the quantum region is composed of three different phases: a normal fluid, a superfluid, and a crystal phase.²⁰ Correspondingly, there exist two triple points, at the upper-left (right) edge of the crystal phase. At high temperature the excitons are in the fluid phase. Cooling leads either into the superfluid or crystal phase. There is no cooling transition from the superfluid to the crystal.

At low densities cooling always leads into the superfluid phase; the transition is accompanied by a sudden increase of γ_s from zero to a finite value. The phase boundary is substantially below the upper limit $T_{KT}(n_s = n)$, Eq. (24), and is in full agreement with our previous analysis for 2D dipoles,¹⁸ indicating that the exciton interaction is close to a dipole potential. The picture suddenly changes when the density exceeds $na_B^{*2} \approx 0.00078$: the superfluid transition vanishes and, instead, a strong modulation of the PDF is observed signaling crystallization, cf. top row of Fig. 2. The critical density corresponds to a dipole coupling parameter $D^c = 17 \pm 1$, which agrees with studies of pure 2D dipole systems.^{17,37} Note that the freezing temperature changes nonmonotonically exhibiting a maximum value T^{\max} around $na_B^{*2} \approx 0.002$.

The superfluid-solid transition is verified by simulating compression along several isotherms. At low temperature and low density, the superfluid fraction γ_s starts from a high value until it suddenly drops to zero at the critical density $na_B^{*2} \approx 0.00078$, cf. bottom part of Fig. 4. This behavior persists up to zero temperature; cf. Fig. 6. Vanishing of quantum coherence upon crystallization is a general feature in this system and indicates that there is *no supersolid phase of indirect excitons*. If the temperature is above the left triple point the superfluid fraction is exactly zero, and compression leads to a phase transition from the normal fluid to the crystal phase, cf. γ_s for $T = 0.001 Ha^*$ and the change of the PDF in Figs. 4(a)–4(c).

D. Reentrant quantum melting

Interestingly, if the density is increased further, the exciton crystal melts, cf. Figs. 4(e) and 4(f), this time accompanied by a jump of the superfluid fraction from zero to about 0.9. This indicates isothermal quantum melting to a (partially) superfluid exciton liquid. This occurs at a density of $nc_a_B^{*2} = 0.0036 \pm 0.0003$ corresponding to $r_s^c = 9.4 \pm 0.3$ and, again, persists to zero temperature. At temperatures above the right triple point, $k_B T \gtrsim 0.001 Ha^*$, melting and onset of superfluidity are decoupled: first the crystal melts into a normal fluid, which becomes a superfluid only at a higher density; cf. Fig. 6.

Thus the most striking feature of the exciton phase diagram is the existence of *two quantum freezing (melting) transitions*, even in the ground state. At low density excitons undergo *pressure crystallization*, which is characteristic for the behavior of dipole systems or, more generally, for neutral matter composed of atoms or molecules. In addition, at higher densities, there is a second transition: *quantum melting* by compression. While such an effect is absent in conventional neutral matter it is ubiquitous in Coulomb systems, including the Wigner crystal of the strongly correlated electron gas, ion crystals in the

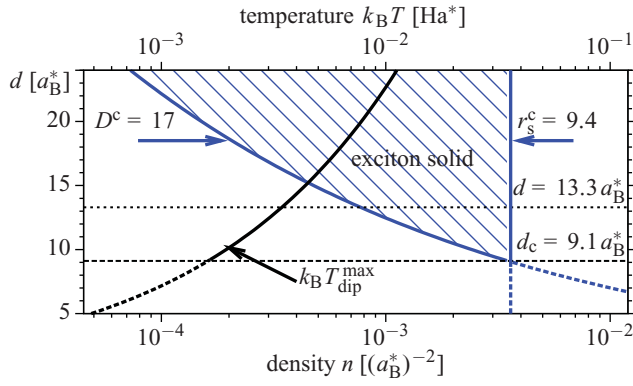


FIG. 7. (Color online) Boundaries of the exciton crystal for different dipole moments d . Lower abscissa: density range given by $D^c = 17$ and $r_s^c = 9.4$. Upper abscissa: maximum temperature estimated from $T_{\text{dip}}^{\text{max}}$. No solid phase exists for $d \leq d_c \approx 9.1a_B^*$.

core of white dwarf stars, and nuclear matter in the crust of neutron stars. The existence of this quantum melting transition in indirect excitons is due to the peculiar shape of the effective potential V_{XX} : one readily confirms in Fig. 1 that at the critical density where the mean exciton-exciton distance equals $9.4a_B^*$, V_{XX} essentially follows the Coulomb repulsion of the holes (red dashed curve).

V. CONCLUSIONS

We have shown that a bosonic many-particle system possesses, besides its weakly nonideal Bose condensed gas and its superfluid liquid phases, also a strongly correlated solid phase. Indirect excitons in semiconductor quantum wells have been found a favorable candidate due to their long-range pair interaction and the possibility to achieve strong nonideality by controlling the dipole moment with an external electric field. Based on first-principles PIMC simulations we have computed the complete phase diagram in the region of the exciton crystal. (Quasi-)long-range crystalline order and macroscopic quantum coherence are found to be incompatible in an exciton crystal—there is no supersolid phase, as long as the crystal is free of defects.

A. Experimental realization

The results presented above were computed for $d = 13.3a_B^*$. Using values from Ref. 21 this dipole moment can be achieved in a ZnSe quantum well of width $L \approx 50$ nm or a GaAs quantum well with $L \approx 148$ nm, both at an electric-field strength of $E = 20$ kV/cm. The density interval for the exciton crystal is estimated as $1.3 \times 10^9 - 3.6 \times 10^9 \text{ cm}^{-2}$ for GaAs and $8.2 \times 10^9 - 3.8 \times 10^{10} \text{ cm}^{-2}$ for ZnSe. An estimate for the maximum temperature where the crystal can exist is obtained from the classical dipole melting curve,

$$k_B T_{\text{dip}} = c \frac{d^2}{a_B^{*2}} (na_B^{*2})^{3/2} \text{ Ha}^*, \quad (26)$$

where $c \approx 0.09$,³⁸ and the critical density $n_C a_B^{*2} = 0.0036$ is being used. Taking into account that this value is approximately a factor 2 too high, cf. Fig. 6, we obtain the estimates $k_B T^{\text{max}} = 0.17$ K (GaAs) and $k_B T^{\text{max}} = 0.78$ K

(ZnSe). These parameters are well within reach of current experiments. A particular advantage is that the upper density limit for exciton crystallization is a factor 16 higher than the threshold for an electron Wigner crystal ($r_s \approx 37$). A suitable diagnostics for the excitonic crystalline phase can be Bragg scattering.¹⁵

B. Dependence of phase diagram on the quantum well width

Let us now analyze the dependence of the phase diagram on the dipole moment d . In semiconductor quantum wells the dipole moment can be varied in a broad range by varying the QW width or/and the electric-field strength. As shown in Fig. 7, an increase of d reduces the lower density limit of the crystal phase whereas the upper boundary remains unchanged. Thus the crystal phase expands with d , the maximum temperature T^{max} grows quadratically, cf. Eq. (26) and Fig. 7. Finally, there exists a minimum value $d_c = 9.1a_B^*$ where the two limiting densities converge, and the exciton crystal phase vanishes.

C. Outlook

Let us now briefly discuss effects which have been neglected by the present model, most importantly, disorder and thermal relaxation. To reduce the effect of the exciton localization at surface imperfections we considered the model of a single wide QW ($L > 400$ Å). This allows us to completely neglect the effect of 1 monolayer well width fluctuations on the exciton binding energy and localization. Some quantitative analysis can be found in Filinov *et al.*³⁹ In our case, the in-plane size of the exciton wave function is comparable to the dipole moment $d = 13.3a_B^* \approx 400$ Å and is therefore of the order of the characteristic lateral size of the interface fluctuations ~ 400 Å (see Gammon *et al.*⁴⁰). Hence once the exciton is on the top of the defect, the corresponding potential gets significantly smoothed.

In many optical experiments excitons are created in a highly nonequilibrium state with a possible coherence and coupling to the laser field. Such conditions, certainly, complicate both the interpretation of the experiment and the theoretical description, and have been studied in detail for polaritons. In contrast, we consider an experimental realization, where the excitons are created by an optical pulse, which is switched off after a short duration, or is periodically repeated with a delay of several microseconds, sufficient for the exciton equilibration. Fast exciton recombination is prevented by the spatial e-h separation due to a constantly applied electric field. This situation is experimentally feasible as was shown by Vörös *et al.*⁴¹

Finally, the most striking feature of the crystal of indirect excitons, confirmed by the simulations, is two quantum melting transitions which persist at zero temperature: at low densities it melts by expansion whereas at high densities it melts when being compressed. The origin of this unusual and rich phase diagram has been traced to the nontrivial form of the exciton interaction potential. With it the exciton solid combines features of conventional neutral matter (exhibiting crystallization by compression^{42,43}) and Coulomb matter (quantum melting by compression), as found, for instance, in exotic compact stars.

ACKNOWLEDGMENTS

We thank D. Hochstuhl for performing multiconfiguration Hartree-Fock calculations for the exciton interaction energy.

Stimulating discussions with Yu. Lozovik and P. Ludwig and financial support by the Deutsche Forschungsgemeinschaft (Project No. FI 1252/1 and SFB-TR24 Project No. A5) are gratefully acknowledged.

*filinov@theo-physik.uni-kiel.de

†bonitz@physik.uni-kiel.de

¹M. H. Anderson, J. R. Ensher, M. R. Matthews, C. E. Wieman, and E. A. Cornell, *Science* **269**, 198 (1995).

²L. V. Butov, C. W. Lai, A. L. Ivanov, A. C. Gossard, and D. S. Chemla, *Nature (London)* **417**, 47 (2002).

³A. H. MacDonald and E. H. Rezayi, *Phys. Rev. B* **42**, 3224 (1990).

⁴L. Tiemann, W. Dietsche, M. Hauser, and K. von Klitzing, *New J. Phys.* **10**, 045018 (2008).

⁵J. Kasprzak *et al.*, *Nature (London)* **443**, 409 (2006).

⁶A. Amo, J. Lefrere, S. Pigeon, C. Adrados, C. Ciuti, I. Carusotto, R. Houdre, E. Giacobino, and A. Bramati, *Nat. Phys.* **5**, 805 (2009).

⁷Y. E. Lozovik and O. L. Berman, *JETP* **84**, 1027 (1997).

⁸A. V. Filinov, M. Bonitz, and Y. E. Lozovik, *J. Phys. A* **36**, 5899 (2003).

⁹A. Filinov, M. Bonitz, P. Ludwig, and Y. E. Lozovik, *Phys. Status Solidi C* **3**, 2457 (2006).

¹⁰V. B. Timofeev and A. V. Gorbunov, *J. Appl. Phys.* **101**, 081708 (2007).

¹¹P. Ludwig, A. V. Filinov, M. Bonitz, and H. Stolz, *Phys. Status Solidi B* **243**, 2363 (2006).

¹²P. Domokos and H. Ritsch, *Phys. Rev. Lett.* **89**, 253003 (2002).

¹³S. Gopalakrishnan, B. L. Lev, and P. M. Goldbart, *Nat. Phys.* **5**, 845 (2009).

¹⁴A. Griesmaier, J. Werner, S. Hensler, J. Stuhler, and T. Pfau, *Phys. Rev. Lett.* **94**, 160401 (2005).

¹⁵K. Sperlich, P. Ludwig, A. Filinov, M. Bonitz, H. Stolz, D. Hommel, and A. Gust, *Phys. Status Solidi C* **6**, 551 (2009).

¹⁶S. De Palo, F. Rapisarda, and G. Senatore, *Phys. Rev. Lett.* **88**, 206401 (2002).

¹⁷G. E. Astrakharchik, J. Boronat, I. L. Kurbakov, and Y. E. Lozovik, *Phys. Rev. Lett.* **98**, 060405 (2007).

¹⁸A. Filinov, N. V. Prokof'ev, and M. Bonitz, *Phys. Rev. Lett.* **105**, 070401 (2010).

¹⁹An alternative realization are two coupled n - and p -doped semiconductor layers.

²⁰At densities exceeding the Mott density n^M pressure ionization transforms the system into an electron-hole plasma. Here additional phases such as a hole liquid or a hole crystal are possible (Ref. 42). However, the present analysis is restricted to densities substantially below the Mott density (Ref. 23).

²¹A. Filinov, P. Ludwig, M. Bonitz, and Y. E. Lozovik, *J. Phys. A* **42**, 214016 (2009).

²²Spatial separation of electrons and holes gives rise to spin polarization at low temperatures (Ref. 23).

²³S. Ben-Taboude Leon and B. Laikhtman, *Phys. Rev. B* **67**, 235315 (2003).

²⁴C. Schindler and R. Zimmermann, *Phys. Rev. B* **78**, 045313 (2008).

²⁵This value of the exciton dipole moment has been predicted theoretically to be achievable in a 40-nm-wide ZnSe single quantum well (Refs. 11 and 21).

²⁶G. Kelbg, *Ann. Phys.* **12**, 219 (1963).

²⁷A. Filinov, M. Bonitz, and W. Ebeling, *J. Phys. A* **36**, 5957 (2003).

²⁸A. V. Filinov, V. O. Golubnychiy, M. Bonitz, W. Ebeling, and J. W. Dufly, *Phys. Rev. E* **70**, 046411 (2004).

²⁹As we consider low temperatures ($T \lesssim 0.01$ Ha*) for the electrons, only the ground-state solution is included. This is due to the large energy gap to the first excited state.

³⁰R. Storer, *J. Math. Phys.* **9**, 964 (1968).

³¹A. Klemm and R. Storer, *Aust. J. Phys.* **26**, 43 (1973).

³²M. Boninsegni, N. V. Prokof'ev, and B. V. Svistunov, *Phys. Rev. E* **74**, 036701 (2006).

³³K. J. Strandburg, *Rev. Mod. Phys.* **60**, 161 (1988).

³⁴P. Hartmann, A. Douglass, J. C. Reyes, L. S. Matthews, T. W. Hyde, A. Kovács, and Z. Donkó, *Phys. Rev. Lett.* **105**, 115004 (2010).

³⁵D. R. Nelson and J. M. Kosterlitz, *Phys. Rev. Lett.* **39**, 1201 (1977).

³⁶D. M. Ceperley, *Rev. Mod. Phys.* **67**, 279 (1995).

³⁷H. P. Büchler, E. Demler, M. Lukin, A. Micheli, N. Prokof'ev, G. Pupillo, and P. Zoller, *Phys. Rev. Lett.* **98**, 060404 (2007).

³⁸R. K. Kalia and P. Vashishta, *J. Phys. C* **14**, L643 (1981).

³⁹A. V. Filinov, C. Riva, F. M. Peeters, Y. E. Lozovik, and M. Bonitz, *Phys. Rev. B* **70**, 035323 (2004).

⁴⁰D. Gammon, E. S. Snow, B. V. Shanabrook, D. S. Katzer, and D. Park, *Phys. Rev. Lett.* **76**, 3005 (1996).

⁴¹Z. Vörös, D. W. Snoke, L. Pfeiffer, and K. West, *Phys. Rev. Lett.* **97**, 016803 (2006).

⁴²M. Bonitz, V. S. Filinov, V. E. Fortov, P. R. Levashov, and H. Fehske, *Phys. Rev. Lett.* **95**, 235006 (2005); *J. Phys. A: Math. Gen.* **39**, 4421 (2006).

⁴³A. Filinov, M. Bonitz, and Yu. Lozovik, *Phys. Rev. Lett.* **86**, 3851 (2001); *Phys. Stat. Sol. (b)* **221**, 231 (2000).